frontiers | Frontiers in Environmental Science

ORIGINAL RESEARCH
published: 25 May 2022
doi: 10.3389/fenvs.2022.925205

Highly Effective Lead Ion Adsorption by Manganese-Dioxide-Supported Core-Shell Structured Magnetite

*Haipeng Zhang, Shiyong Chen, Yuhua Shan, Xiaoqing Qian, Yanju Yang and Juanjuan Wang**

Key Laboratory of Cultivated Land Quality Monitoring and Evaluation, Ministry of Agriculture and Rural Affairs, College of Environmental Science and Engineering, Yangzhou University, Yangzhou, China

In this research, a magnetic core-shell composite, consisting of a Fe_3O_4 core and a silica shell (called Fe_3O_4@SiO_2), was developed and then functionalized via MnO_2 grafting at different MnO_2 deposition levels (termed Fe_3O_4@SiO_2-MnO_2). The resulting materials were characterized by X-ray fluorescence, X-ray diffraction, a vibration sample magnetometer, transmission electron microscopy, N_2 adsorption-desorption, zeta-potential studies and X-ray photoelectron spectroscopy. Visualizations showed that Fe_3O_4@SiO_2-MnO_2 had a magnetite core with size of 100 nm, overlaid by a rough silica shell and a relatively loose MnO_2 deposition. The Pb(II) adsorption onto the composites was also assessed. It was found that MnO_2 deposition on the Fe_3O_4@SiO_2 surface enhanced Pb(II) adsorption, and the Pb(II) adsorption amount was highly correlated to the MnO_2 deposition level. The adsorption kinetics of Pb(II) followed pseudo-second-order kinetics, and the adsorption rate could be decreased by increasing the initial concentration of Pb(II). A higher pH resulted in enhanced Pb(II) adsorption, which slightly increased with the coexistence of Na^+ and Ca^{2+}, along with the presence of dissolved humic acid. The adsorbent could easily be separated and recovered under the action of the external magnetic component and it displayed stable adsorption behaviour over four adsorption-desorption periods. The results emphasize the high potential of Fe_3O_4@SiO_2-MnO_2 materials for the adsorptive removal of Pb(II) in water.

Keywords: lead removal, adsorption, Fe_3O_4@SiO_2, MnO_2 grafting, water treatment

OPEN ACCESS

Edited by:
Shihai Deng,
Xi'an Jiaotong University, China

Reviewed by:
Haiqin Wan,
Nanjing University, China
Mazaher Ahmadi,
Bu-Ali Sina University, Iran

****Correspondence:***
Juanjuan Wang
wangjuanjuan@yzu.edu.cn

Specialty section:
This article was submitted to Water and Wastewater Management, a section of the journal Frontiers in Environmental Science

Received: *21 April 2022*
Accepted: *12 May 2022*
Published: *25 May 2022*

Citation:
Zhang H, Chen S, Shan Y, Qian X, Yang Y and Wang J (2022) Highly Effective Lead Ion Adsorption by Manganese-Dioxide-Supported Core-Shell Structured Magnetite. Front. Environ. Sci. 10:925205. doi: 10.3389/fenvs.2022.925205

INTRODUCTION

Lead (Pb(II)) pollutant in municipal and industrial wastewater poses a serious threat to public health and ecological systems (Liu et al., 2018). Different treatment techniques, involving chemical precipitation (Li et al., 2022), ion exchange (Li et al., 2017), adsorption (Hussain et al., 2021), and membrane separation (Hamid et al., 2020), have been used to eliminate Pb(II) pollution, among which adsorption has the highest removal efficiency and ease of operation. Therefore, the design and preparation of effective adsorbents for aqueous Pb(II) removal are being widely researched.

Some metal oxides–such as Fe_2O_3, Al_2O_3, and MnO_2–have been evaluated for adsorbing Pb(II) from wastewaters, among which MnO_2 has exhibited promising potential for the adsorptive removal of Pb(II) (Zhang et al., 2020b; Yadav et al., 2021; Ghaedi et al., 2022). Zhang et al. (2017a) and Li et al. (2021) found that MnO_2 presented a strong affinity for Pb(II) under acidic conditions and played a significant role in controlling the geochemical cycle of heavy metal ions owing to its high specific surface area and negatively charged surface over an extensive pH range. However, pure nanosized

MnO_2 particles tend to aggregate in water. The separation of MnO_2 nanoparticles requires energy-intensive filtration, increasing the total cost and leading to filter clogging (Zhu et al., 2015).

Magnetic separation is quicker and more efficient than traditional filtration when used to separate suspended magnetic particles (Xia and Liu, 2021). Fe_3O_4 and γ-Fe_2O_3 are common magnetic agents, exhibiting superparamagnetic behaviour and strong magnetization. Combining their magnetic efficacy with that of MnO_2 nanoparticles can help mitigate the limitation of MnO_2 nanoparticles in terms of their slow separation from water. However, magnetic Fe_3O_4 and γ-Fe_2O_3 are not stable under acidic conditions (Bandar et al., 2021). Significant research effort has been devoted to enhancing the stability of magnetic iron oxides by coating them with polymers (Chen et al., 2018), lauric acid (Zhu et al., 2019), carbon (Wang W. et al., 2015), ZrO_2 (Gugushe et al., 2021) and SiO_2 (Vishnu and Dhandapani, 2020). Notably, SiO_2-based coatings are very stable under acidic conditions and highly resistant to oxidants and reductants (Vishnu and Dhandapani, 2020). Hence, they can act as ideal shell composites to shield the inner magnetic cores. Furthermore, SiO_2 has a high specific surface area and abundant hydroxyl groups, which facilitates facile functionalization. For instance, Huang et al. (2014) used M-Fe_3O_4@SiO_2/ZnO for the photocatalytic degradation of methyl group, finding that SiO_2 incorporation prevented the agglomeration of the Fe_3O_4 nanoparticles and enhanced the photocatalytic performance. Vishnu and Dhandapani (2020) synthesized an amino-functionalised silica-coated magnetic nanoparticle with high stability under acidic conditions. However, there have been few reports on the incorporation of MnO_2 onto the surface of magnetic core-shell nanoparticles. Zhang et al. (2015) prepared a Fe_3O_4@SiO_2@MnO_2 composite as an adsorbent for the decolouration of methyl orange, which consisted of a magnetic Fe_3O_4 core, SiO_2 shell–with thickness of 40 nm–and MnO_2 nanoparticles adhering to the surface of SiO_2 body, with a diameter of about 10 nm. However, the thick SiO_2 body and large MnO_2 nanoparticles decreased the saturation magnetisation (M_s) of Fe_3O_4 from 82.47 emu g^{-1}–29.41 emu g^{-1}, which markedly restricted the efficiency of magnetic separation and recovery of the adsorbent. Hence, we hypothesize that a nanocomposite of Fe_3O_4 core, a thin SiO_2 shell and a monolayer of active MnO_2 will exhibit a high adsorption ability and separability for Pb(II). However, to the best of our knowledge, no such study has been reported to date.

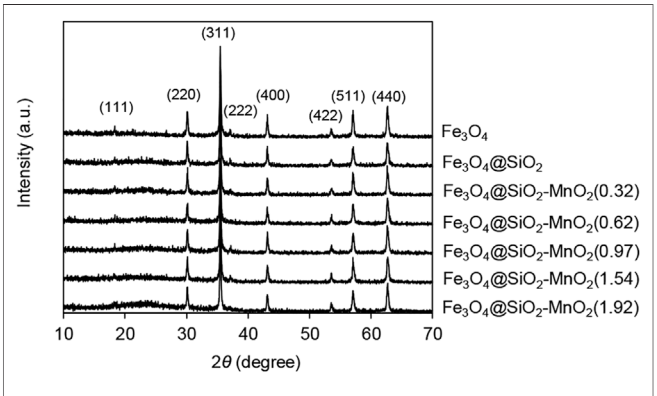

FIGURE 1 | XRD patterns of the samples.

Magnetic nano-adsorbents were synthesized in this study by grafting MnO_2 with various of concentrations onto the surface of Fe_3O_4@SiO_2 core-shell nanoparticles. The characterization of the adsorbents included X-ray fluorescence (XRF), powder X-ray diffraction (XRD), transmission electron microscopy (TEM), vibration sample magnetometry (VSM), N_2 adsorption-desorption, X-ray photoelectron spectroscopy (XPS) and zeta-potential tests. The Pb(II) adsorption capabilities of the materials including the adsorption ability, kinetics, the impact of water chemistry on adsorption, and the regeneration of the saturated adsorbents, were investigated to evaluate the performance of the novel adsorptive materials.

MATERIALS AND METHODS

Adsorbent Preparation

The Fe_3O_4 nanoparticles were prepared using the procedure described by Huang et al. (2014) and Shi et al. (2021). In brief, 3.0 g of $FeCl_3 \cdot 6H_2O$, 2.0 g of polyvinylpyrrolidone and 7.2 g of sodium acetate were dissolved in 60 ml ethylene glycol at 50°C. This was followed by transferring the compound to a 100 ml stainless steel autoclave lined with Teflon and heating it to 200°C for 8 h. Once the mixture' temperature dropped to room temperature, the black solid was gathered through magnetic separation, repeatedly washed in ethanol and deionized water, and then dried at 60°C in a vacuum for 12 h.

After dispersing 1.0 g of Fe_3O_4 nanoparticles in 200 ml of deionized water at 80°C, 20 ml of 1.0 mol L^{-1} Na_2SiO_3 solution was added to the suspension with vigorous agitation. The pH was adjusted to 6.0 using 2.0 mol L^{-1} HCl solution within 1 h, followed by 3 h of vigorous agitation at 80°C. It was necessary to utilize magnetic separation to collect the resulting nanoparticles, which were then thoroughly washed with deionized water, and followed by drying for 12 h in a vacuum at 60°C. The material obtained is referred to as Fe_3O_4@SiO_2.

$KMnO_4$ as the source of manganese was used to prepare MnO_2-functionalized Fe_3O_4@SiO_2 nanoparticles. One gram of Fe_3O_4@SiO_2 nanoparticles was suspended in 100 ml of deionized water, and the predicted amount of $KMnO_4$ solution was added. The mixture was then added dropwise to 40 ml of 30% H_2O_2 solution. Within 0.5 h of mechanical stirring, the pH of this solution was adjusted to 7.0 by adding 1.0 mol L^{-1} HNO_3. Following that, the reaction mixture was agitated at 25°C for 3 h. The final compound was collected through magnetic separation and repeatedly washed with deionized water before drying at 60°C in a vacuum for 12 h. The subsequent components were designated as Fe_3O_4@SiO_2-MnO_2(X), where X denotes the concentration of MnO_2 (wt. per cent).

TABLE 1 | BET surface areas and contents of Fe_3O_4, SiO_2 and MnO_2 of the sorbents.

Sample	Content ratio[a] %			S_{BET} (m^2 g^{-1})
	Fe_3O_4	SiO_2	MnO_2	
Fe_3O_4@SiO_2	54.24	45.76	—	27.2
Fe_3O_4@SiO_2-MnO_2(0.32)	55.15	44.53	0.32	32.1
Fe_3O_4@SiO_2-MnO_2(0.62)	54.57	44.81	0.62	36.1
Fe_3O_4@SiO_2-MnO_2(0.97)	55.32	43.71	0.97	35.0
Fe_3O_4@SiO_2-MnO_2(1.54)	53.66	44.80	1.54	36.6
Fe_3O_4@SiO_2-MnO_2(1.92)	54.31	43.77	1.92	38.4

[a]*Determined by X-ray fluorescence.*

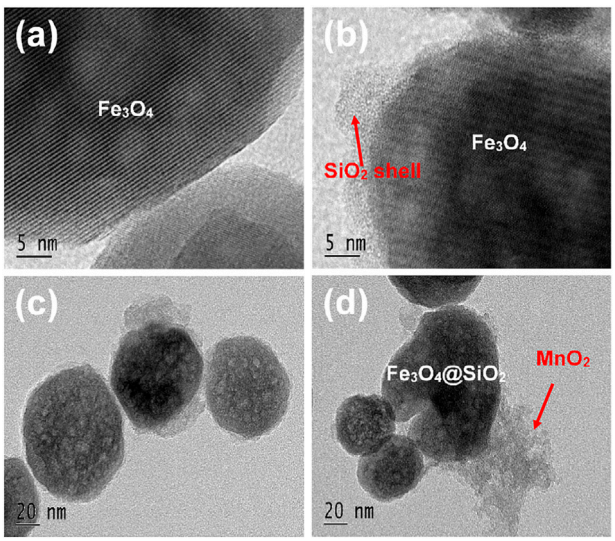

FIGURE 2 | TEM images of **(A)** Fe_3O_4, **(B)** Fe_3O_4@SiO_2, and **(C,D)** Fe_3O_4@SiO_2-MnO_2(1.54).

Material Characterization

The amount of MnO_2 present in the adsorbents was measured using an ARL9800XP X-ray fluorescence (XRF) spectrometer (Thermo Electron, Switzerland). The X-ray diffraction (XRD) patterns of the materials were recorded using a Rigaku *D*/max-RA powder diffractometer connected to a Cu Kα radiation source over a wide range of angles (10–70°) (Rigaku, Japan). An electron microscopy, the JEM-2100 (JEM-2100, JEOL, Japan), was utilized to analyse the morphology of the adsorbents under investigation. Through the N_2 adsorption-desorption operations performed on a Micromeritics ASAP 2020 analyser (Micromeritics Instrument Co., Norcross, GA, United States), we evaluated the Brunauer–Emmett–Teller (BET) surface area at −196°C (77 K). In this study, an XPS examination was carried out using a PHI5000 VersaProbe equipped with a monochromatized Al Kα excitation source ($h\nu$ = 1,486.6 eV) (ULVAC-PHI, Japan). The binding energy was calibrated using the C 1s peak (284.6 eV). A vibrating sample magnetometer was used to determine the magnetic characteristics of the sample (Lake Shore VSM 7410, United States). A Zeta Potential Analyser was utilized to determine the nanoparticles' surface Zeta (ζ) potentials (Zeta PALS, Brookhaven Instruments Co., United States). To ensure proper dispersion 24 h before the zeta potential measurement, 40 mg of the material was spread evenly across 400 ml of 1.0 mmol L^{-1} $NaNO_3$ solution, and various solution pH values were obtained by adding 0.1 mol L^{-1} HNO_3 or NaOH.

Batch adsorption Experiments

We determined the Pb(II) adsorption isotherms by conducting a series of batch adsorption tests. A 40 ml glass vial was filled with 40 ml of Pb(II) solution with various initial concentrations and capped with a screw cap containing 20.0 mg of adsorbent. The pH of the combination was maintained at 4.0 ± 0.2. The samples were then oscillated in an orbital shaker at 25°C for 24 h. Preliminarily kinetic trials (data available upon reasonable request) indicated that the adsorption time (24 h) was sufficient to reach an apparent adsorption equilibrium. Following the equilibrium adsorption, the adsorbent was magnetically isolated from the aqueous solutions. When determining the residual Pb(II) concentrations in aliquots, atomic absorption spectroscopy (AAS) (Hitachi Z-8100, Japan) was utilized. The equilibrium amount (mg g^{-1}) of Pb(II) adsorption was determined as following:

$$q_e = \frac{(C_0 - C_e)V}{M} \tag{1}$$

The initial and equilibrium concentrations of Pb(II) are C_0 and C_e (mg L^{-1}), respectively. The total volume of Pb(II) solution is V (L) and the adsorbent mass M is measured in grams.

The Pb(II) adsorption data were fitted to the Langmuir and Freundlich models, which were often used to describe the interaction between the adsorbate and the adsorbent. The Langmuir and Freundlich models could be expressed as **Eqs. 2**, **3**, respectively:

$$\frac{C_e}{q_e} = \frac{C_e}{q_m} + \frac{1}{q_m b} \tag{2}$$

$$\log q_e = \log K_f + \frac{1}{n}\log(C_e) \tag{3}$$

The maximum adsorption capacity is represented by q_m (mg g^{-1}), and b (L mg^{-1}) is the Langmuir equilibrium constant. K_f (mg g^{-1}) is the Freundlich coefficient, which indicates the adsorbent's adsorption capacity, and n is the linearity index, which indicates the adsorption intensity.

Adsorption Kinetics

To investigate the Pb(II) adsorption kinetics, 250.0 mg of Fe_3O_4@SiO_2-MnO_2(1.54) was put into a round-bottom flask with 500 ml of aqueous solution with different Pb(II) concentrations (10.0 mg L^{-1} and 25.0 mg L^{-1}) under vigorous stirring. About 5 ml of the solution was sampled using a pipette at preset time separations. The suspended magnetic nanoparticles were fast filtered by a 0.22 μm filter membrane. AAS was used to determine the concentration of Pb(II) in the filtrate. The

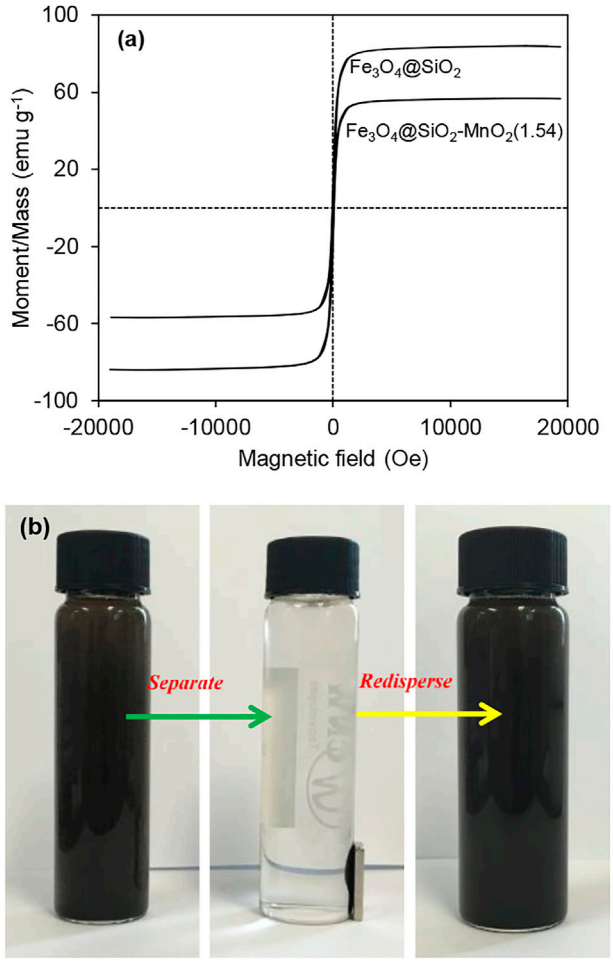

FIGURE 3 | (A) Magnetization curves of Fe_3O_4@SiO_2 and Fe_3O_4@SiO_2-MnO_2(1.54) and **(B)** the magnetic separation and redispersion of Fe_3O_4@SiO_2-MnO_2(1.54).

quantity of Pb(II) adsorption was calculated using the following formula:

$$q_t = \frac{(C_0 - C_t)V}{M} \tag{4}$$

An adsorbing quantity, known as "q_t" (mg g^{-1}) is dependent on t (min). C_0 and C_t are the Pb(II) solution concentration (mg L^{-1}) at initial and time t of (mg L^{-1}). The volume of Pb(II) solution is measured by V (L) and the adsorbent mass M is measured in grams.

Effect of Water Chemistry on Pb(II) adsorption

Using Fe_3O_4@SiO_2-MnO_2(1.54) at a temperature of 25°C, the influence of pH on Pb(II) adsorption was investigated. A 25.0 mg L^{-1} Pb(II) solution with variable pH was added to Teflon-lined, cap-on glass tubes containing 20.0 mg of Fe_3O_4@

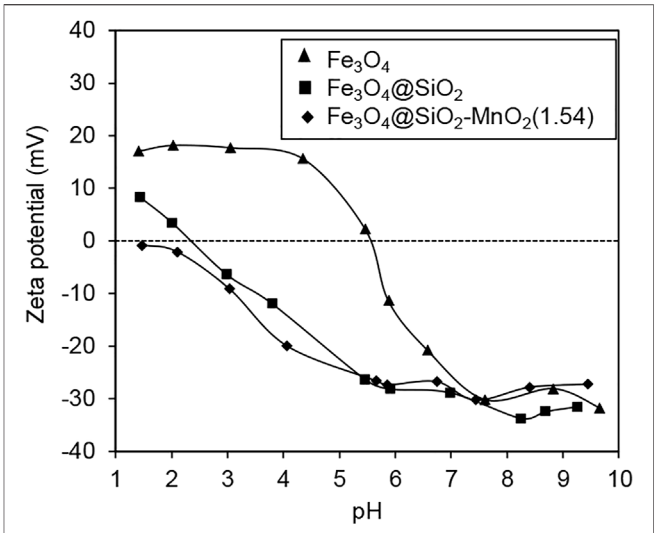

FIGURE 4 | Surface zeta potentials of the samples as a function of pH.

SiO_2-MnO_2(1.54), and the tubes were shaken at 25°C for 48 h. **Equation 1** was used to compute the amount of Pb(II) adsorption, and the residual Pb(II) concentration was evaluated by AAS. The effects of co-existing ions on Pb(II)

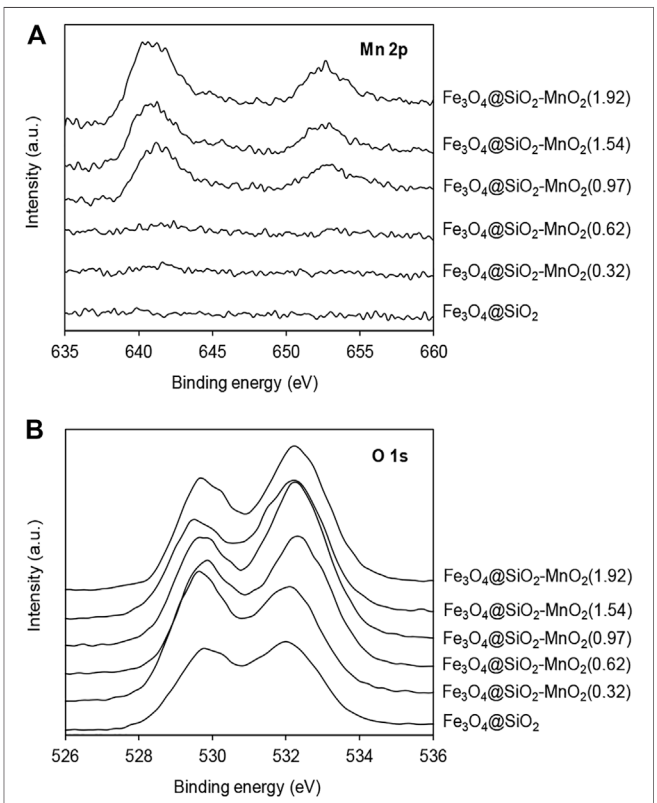

FIGURE 5 | XPS spectra of Fe_3O_4@SiO_2 and Fe_3O_4@SiO_2-MnO_2 in **(A)** the Mn 2p and **(B)** the O 1s region.

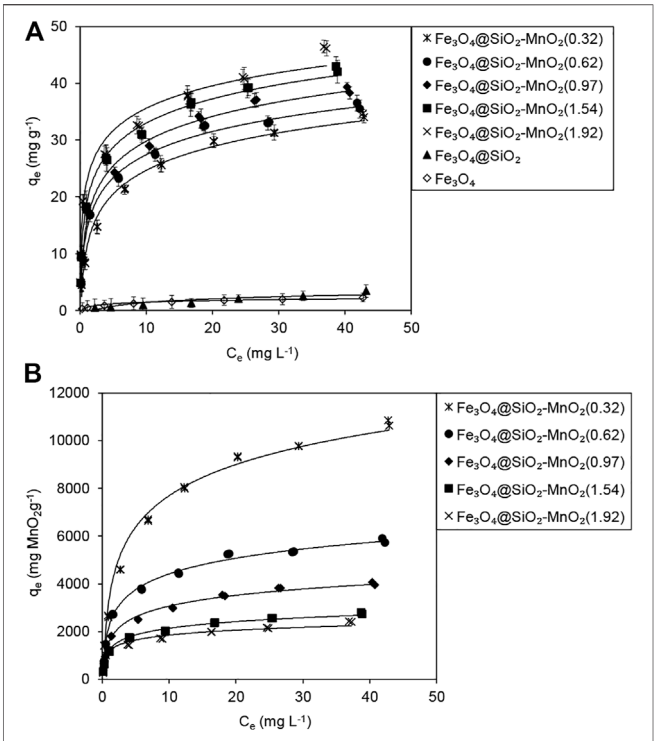

FIGURE 6 | (A) Pb(II) adsorption isotherms and **(B)** MnO_2 content-normalized Pb(II) adsorption isotherms of the samples. (Adsorbent dosage = 0.5 g L^{-1}, Temperature = 25°C, pH = 4.0 ± 0.2).

adsorption onto Fe_3O_4@SiO_2-MnO_2(1.54) were carried out with the presence of various NaCl or $CaCl_2$ concentrations (0.01–0.20 mol L^{-1}) at pH 4.0 ± 0.2, and at 25°C. The effect of dissolved humic substances on Pb(II) adsorption was studied by comparing the adsorption isotherms of Pb(II) in the presence and absence of dissolved humic acid (Sigma-Aldrich) at a concentration of 10.2 mg L^{-1}.

Desorption and Regeneration of the Saturated Adsorbent

To determine the reusability of the synthesized sorbent, eight successive periods of Pb(II) adsorption and regeneration on Pb(II)-saturated Fe_3O_4@SiO_2-MnO_2 (1.54) were conducted. Specifically, 50.0 mg of Fe_3O_4@SiO_2-MnO_2(1.54) was suspended in 100 ml of 25.0 mg L^{-1} Pb(II) solution and maintained at 25°C for 24 h with vigorous stirring. The Pb(II)-saturated adsorbent was then split magnetically, and the residual Pb(II) concentration was measured by methods described previously. The resultant Pb(II)-saturated adsorbent was regenerated by suspending it in 20 ml of 1.0 mol L^{-1} HCl solution and keeping it for 24 h. Before the next adsorption-desorption period, the regenerated adsorbent was repeatedly cleaned using deionized water until the pH of the supernatant was almost neutral.

RESULTS AND DISCUSSION

Characterization of the Adsorbents

The XRD diagrams of Fe_3O_4, Fe_3O_4@SiO_2 and Fe_3O_4@SiO_2-MnO_2 with different MnO_2 concentrations are shown in **Figure 1**. The major diffraction peaks of Fe_3O_4 were determined with 2θ of 18.3°, 30.1°, 35.5°, 37.1°, 43.1°, 53.5°, 57.1°, and 62.7°, this indicated the existence of magnetite with a cubic spinel framework (Bandar et al., 2021; Panahandeh et al., 2021). For Fe_3O_4@SiO_2, no prominent and new crystalline peak was observed, revealing that SiO_2 component in Fe_3O_4@SiO_2 was amorphous (Bandar et al., 2021). Upon MnO_2 functionalization, a broad peak at 2θ of 23.7° was detected (except for the diffraction peaks of Fe_3O_4@SiO_2), the intensity of which enhanced with increasing MnO_2 concentration, reflecting the presence of amorphous MnO_2 moieties on the Fe_3O_4@SiO_2 surface (Yin et al., 2011; Zhang et al., 2017b). Additionally, the few diffraction peak features of crystalline MnO_2 reflected the low MnO_2 content in the Fe_3O_4@SiO_2-MnO_2 adsorbents.

The BET surface areas of the adsorbents identified through N_2 adsorption-desorption are summarized in **Table 1**. These specific surface areas of the Fe_3O_4@SiO_2-MnO_2 adsorbents were higher than that of Fe_3O_4@SiO_2, revealing an increase in the surface area upon functionalization. The XRF analysis results of MnO_2 loading amounts are listed in **Table 1**. The MnO_2 contents of Fe_3O_4@SiO_2-MnO_2 adsorbents were 0.32, 0.62, 0.97, 1.54, and 1.92 (wt%), reflecting the successful grafting of MnO_2 onto the Fe_3O_4@SiO_2 surface.

TABLE 2 | Fitting parameters of the Langmuir and Freundlich isotherm models for adsorption of Pb(II) onto the adsorbents.

Adsorbent	Langmuir Model				Freundlich Model		
	b (L mg^{-1})	q_m (mg g^{-1})	Q_m (mg gMnO_2^{-1})	*Adj.* R^2	K_f (mg g^{-1})	*n*	*Adj.* R^2
Fe_3O_4	1.46	1.59	—	0.963	0.51	0.39	0.994
Fe_3O_4@SiO_2	0.55	2.4	—	0.866	0.13	0.85	0.982
Fe_3O_4@SiO_2-MnO_2(0.32)	0.78	26.5	8,290.6	0.965	8.91	2.53	0.976
Fe_3O_4@SiO_2-MnO_2(0.62)	0.83	32.2	5,185.5	0.991	11.01	2.79	0.961
Fe_3O_4@SiO_2-MnO_2(0.97)	0.92	34.0	3,506.2	0.990	11.87	2.75	0.968
Fe_3O_4@SiO_2-MnO_2(1.54)	1.84	33.6	2,179.2	0.994	14.33	2.98	0.975
Fe_3O_4@SiO_2-MnO_2(1.92)	3.70	35.1	1827.6	0.993	17.23	3.40	0.977

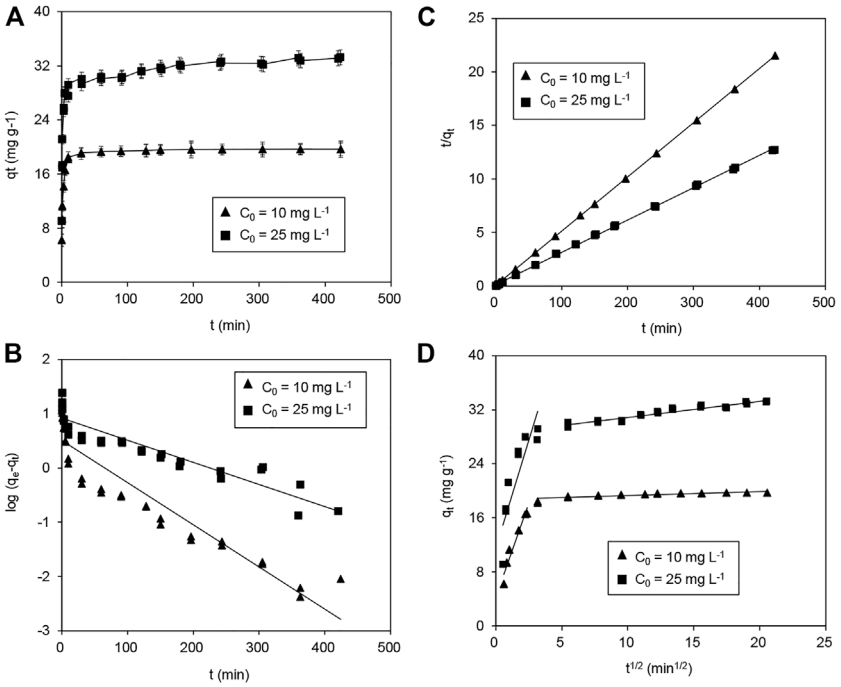

FIGURE 7 | (A) Adsorption of Pb(II) with various initial concentrations on Fe_3O_4@SiO_2-MnO_2(1.54) as a function of the adsorption time, and fitting of Pb(II) adsorption kinetics using the **(B)** pseudo-first-order model, **(C)** pseudo-second-order model and **(D)** Weber-Morris model. (C_0 (Pb(II) = 10.0 mg L^{-1} and 25.0 mg L^{-1}, respectively, adsorbent dosage = 0.5 g L^{-1}, Temperature = 25°C, pH = 4.0 ± 0.2).

The TEM images of Fe_3O_4, Fe_3O_4@SiO_2 and Fe_3O_4@SiO_2-MnO_2 are displayed in **Figure 2**. The Fe_3O_4 image (**Figure 2A**) showed the aggregation of spherical clusters with an average diameter of 100 nm. In **Figure 2B**, rough SiO_2 with a thickness of approximately 3 nm outside the Fe_3O_4 core was identified, reflecting that Fe_3O_4@SiO_2 consists of Fe_3O_4 cores and SiO_2 shells. After MnO_2 functionalization (see **Figures 2A,C,D** relatively loose body was obviously observed on the Fe_3O_4@SiO_2 surface, reflecting the successful deposition of MnO_2 onto the Fe_3O_4@SiO_2 surface.

The magnetization curves determined for Fe_3O_4@SiO_2 and Fe_3O_4@SiO_2-MnO_2(1.54) are presented in **Figure 3A**. The saturation magnetisation (M_s) of Fe_3O_4@SiO_2 was determined to be 84.1 emu g^{-1}, whereas the M_s of Fe_3O_4 nanosphere was reported to around 100.3 emu g^{-1} (Shi et al., 2021). The lower saturation magnetization of Fe_3O_4@SiO_2 than that of Fe_3O_4 could be attributed to the SiO_2 shell. After MnO_2 modification, the saturation magnetization of Fe_3O_4@SiO_2-MnO_2(1.54) continuously reduced to 56.8 emu g^{-1}, further confirming the successful deposition of MnO_2 onto the Fe_3O_4@SiO_2 surface. VSM results also showed that the samples were superparamagnetic with no remanent coercivity (Xu et al., 2018). As evident in **Figure 3B**, the effective separation and recovery of Fe_3O_4@SiO_2-MnO_2(1.54) could be achieved in seconds with the assistance of an external magnetic field. Further, the nanoparticles quickly redispersed while the magnetic field was removed, reflecting the potential for using MnO_2-functionalized Fe_3O_4@SiO_2 magnetic nanoparticles as recyclable adsorbent in water and wastewater treatment.

The surface zeta potentials of Fe_3O_4, Fe_3O_4@SiO_2 and Fe_3O_4@SiO_2-MnO_2(1.54) are displayed in **Figure 4**, as a function of pH. The surface potential gradually decreased with increases in the pH for all of the samples, likely due to the deprotonated surface hydroxyl groups. The isoelectric point (IEP) of the Fe_3O_4 nanoparticles was found to be 5.8, which was in line with the value found in literature (Bandar et al., 2021). The IEP of Fe_3O_4@

TABLE 3 | Fitting parameters of Pb(II) adsorption kinetics on Fe_3O_4@SiO_2-MnO_2(1.54) using pseudo-first-order, pseudo-second-order, and Weber-Morris models.

C_0 mg L^{-1}	q_{exp} mg g^{-1}	Pseudo-first-order			Pseudo-second-order			Weber-Morris Model		
		k_1 min^{-1}	q_{cal} mg g^{-1}	*Adj.* R^2	k_2 g mg^{-1} min^{-1}	q'_{cal} mg g^{-1}	*Adj.* R^2	k_d mg g^{-1} $min^{-1/2}$	*I* g mg^{-1}	*Adj.* R^2
10	19.7	0.018	3.2	0.875	0.049	19.7	0.999	5.49	4.41	0.921
25	33.2	0.011	13.5	0.845	0.006	33.2	0.999	7.53	1.08	0.957

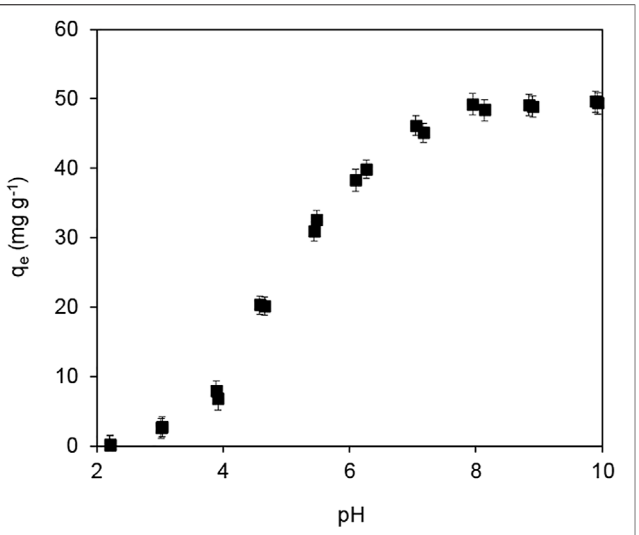

FIGURE 8 | Effect of the solution pH on Pb(II) adsorption by Fe_3O_4@SiO_2-MnO_2(1.54). (C_0 (Pb(II) = 25.0 mg L^{-1}, adsorbent dosage = 0.5 g L^{-1}, Temperature = 25°C).

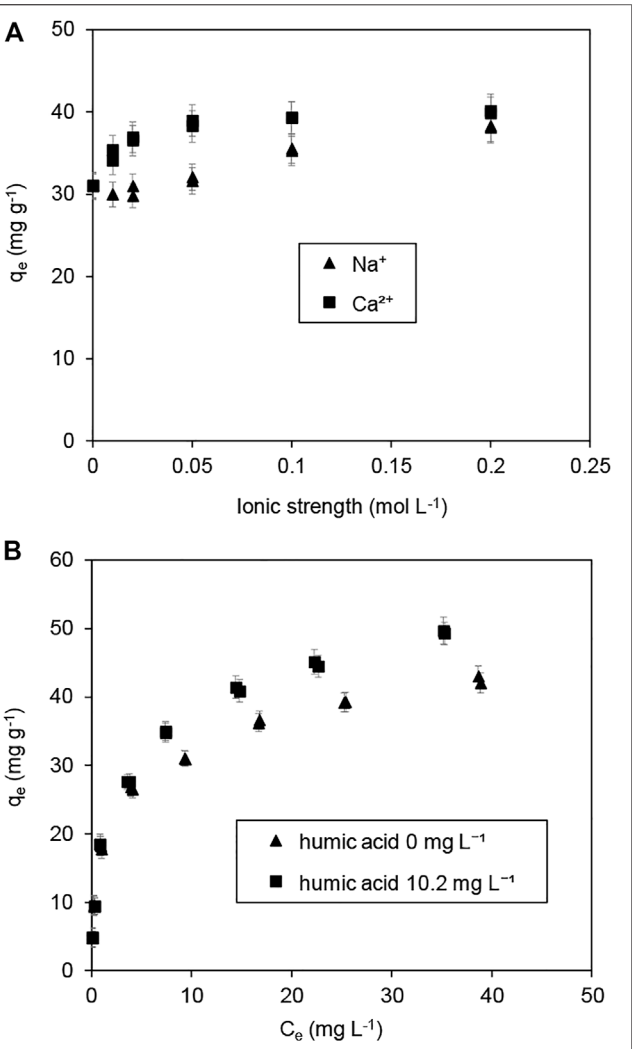

FIGURE 9 | (A) Effect of co-existing ions on Pb(II) adsorption over Fe_3O_4@SiO_2-MnO_2(1.54), and **(B)** adsorption isotherms of Pb(II) on Fe_3O_4@SiO_2-MnO_2(1.54) in the absence and presence of dissolved humic acid. (Adsorbent dosage = 0.5 g L^{-1}, Temperature = 25°C, pH = 4.0 ± 0.2).

SiO_2 was found to be 2.4, further confirming the successful amorphous silica coating (Wang et al., 2013). More specifically, the IEP of Fe_3O_4@SiO_2-MnO_2(1.54) was found to be approximately 1.4. It is important to note that the IEP of MnO_2 has previously been found to lie within the range of 1–2 (McBride, 1997; Huang et al., 2014). Hence, the lower IEP of Fe_3O_4@SiO_2-MnO_2(1.54) compared with Fe_3O_4@SiO_2 was attributed to the MnO_2 grafting on the Fe_3O_4@SiO_2 surface.

The XPS spectra of Mn 2p and O 1s are presented in **Figures 5A,B**, respectively. In the spectra of Fe_3O_4@SiO_2-MnO_2 adsorbents, Mn 2p peaks were found, reflecting the successful grafting of the MnO_2 functional groups onto the Fe_3O_4@SiO_2 surface. The typical Mn 2p XPS spectrum of Fe_3O_4@SiO_2-MnO_2 nanoparticles revealed a spin-orbit doublet with Mn $2p_{1/2}$ (653.3 eV) and Mn $2p_{3/2}$ (641.3 eV), which was separated into a mixed-valent manganese system comprising Mn^{3+} and Mn^{4+} (Zhang et al., 2015; Zhang et al., 2017b). Owing to the low MnO_2 content and high MnO_2 dispersion, the intensity of the Mn $2p_{1/2}$ and Mn $2p_{3/2}$ peaks of Fe_3O_4@SiO_2-MnO_2(0.32) and Fe_3O_4@SiO_2-MnO_2(0.62), respectively, were not the typical intensities reported for manganese oxides in literature (Zhang et al., 2020a). In the case of the O 1s spectrum (**Figure 5B**), two peaks at 529.8 and 532.1 eV appeared in the spectra of the samples, indicative of the lattice oxygen (*i.e.*, Mn-O, Si-O and Fe-O) and surface oxygen (O-H) (Wan et al., 2020; Minale et al., 2021), respectively. Additionally, the area ratio of surface oxygen increased with increasing MnO_2 deposition levels, which was ascribed to the abundance of hydroxyl groups on the functionalized manganese oxides (Wang et al., 2013).

Adsorption Isotherms

Figure 6A shows the isotherms of Pb(II) adsorption onto the adsorbents. Very low quantities of Pb(II) adsorption was detected for Fe_3O_4 and Fe_3O_4@SiO_2, indicating that the Fe_3O_4 and Fe_3O_4@SiO_2 exhibited a negligible affinity for Pb(II) adsorption. In comparison to Fe_3O_4 and Fe_3O_4@SiO_2, Fe_3O_4@SiO_2-MnO_2 exhibited a significant increase in Pb(II) adsorption, which increased as the MnO_2 deposition level rose, indicating that MnO_2 was the active species for Pb(II) adsorption.

Table 2 summarizes the fitting parameters. For Fe_3O_4@SiO_2-MnO_2(0.32), the *Adj.* R^2 value (0.976) of the Freundlich model was slightly higher than that of the Langmuir model (0.965), likely because the Fe_3O_4@SiO_2 surface was not entirely covered by MnO_2 at the 0.32% (wt.) deposition level, leading to significant adsorption heterogeneity (Feheem, et al., 2016). In contrast, much higher R^2 values (0.990–0.994) of the Langmuir model were obtained when the MnO_2 deposition levels increased, indicating homogeneous adsorption sites for Pb(II) adsorption at high MnO_2 deposition levels. Additionally, the b and K_f values increased with increasing

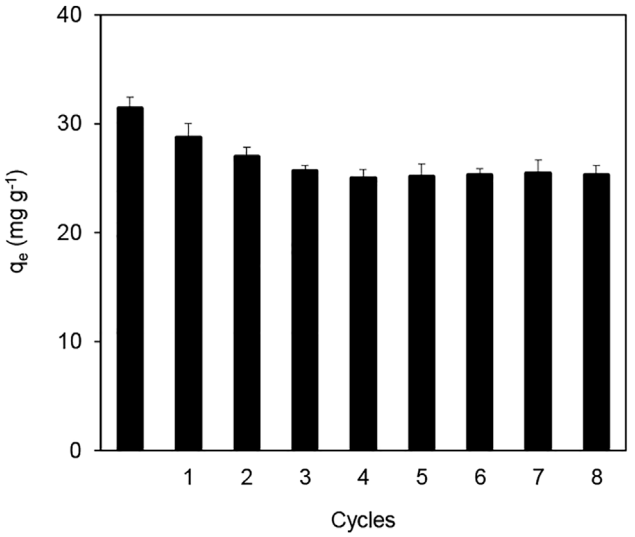

FIGURE 10 | Pb(II) adsorption by virgin and regenerated Fe_3O_4@SiO_2-MnO_2(1.54) adsorbent within eight adsorption-desorption cycles. (C_0 (Pb(II) = 25.0 mg L^{-1}, adsorbent dosage = 0.5 g L^{-1}, Temperature = 25°C, Pb(II) adsorption pH = 4.0 ± 0.2).

MnO_2 deposition levels, confirming that the active adsorption species was MnO_2.

The calculated q_m of the sorbents suggested that Pb(II) adsorption was not strongly affected by the MnO_2 deposition levels. To obtain deeper insight into the adsorption mechanism, MnO_2-content-normalized adsorption isotherms of Fe_3O_4@SiO_2 with various MnO_2 deposition levels are compared in **Figure 6B**. The calculated maximum adsorption capacities Q_m upon MnO_2 content normalization are listed in **Table 2**. For Fe_3O_4@SiO_2-MnO_2 with various MnO_2 contents, the adsorption capacities Q_m decreased with increasing MnO_2 deposition levels, and the highest Q_m was observed for Fe_3O_4@SiO_2-MnO_2(0.32). This is likely due to the high dispersion of nanosized MnO_2 particles at low deposition levels, and thus, the high utilization of MnO_2 as the active site for Pb(II) adsorption. At higher deposition levels, the MnO_2 particles may aggregate, leading to the partial inaccessibility of the adsorption sites. Notably, almost identical adsorption isotherms were acquired for MnO_2 normalization at deposition levels of 1.54 (wt%) and 1.92 (wt%), reflecting similar structural characteristics (*e.g.*, the content of hydroxyl groups and the particle size) (Zhang et al., 2020a). The nearly identical normalized isotherms implied that the outer surface of SiO_2 shell might be entirely covered at the 1.54% (wt.) MnO_2 deposition, which was in good agreement with the XPS results.

MnO_2 is used as an effective adsorbent for Pb(II) removal in wastewater. Wan et al. (2018) found that the maximum adsorption capacity of biochar-supported hydrated manganese oxide for Pb(II) was 23.8 mg g^{-1} at a pH of 4.5. Wang S. et al. (2015) investigated Pb(II) adsorption on MnO_2-modified biochar acquired an adsorption capacity of 47.1 mg g^{-1} at an equilibrium concentration of 40 mg L^{-1}. Note that the adsorption capacity usually increases with the equilibrium concentration of the adsorbate, and these high adsorption capacities reported were obtained at relatively high Pb(II) equilibrium concentrations. In the current research, the maximum adsorption of Pb(II) on Fe_3O_4@SiO_2-MnO_2(1.54) was 33.6 mg g^{-1} Fe_3O_4@SiO_2-MnO_2 at an equilibrium concentration of 24.0 mg L^{-1} and pH of 4.0, showing that the uptake of Pb(II) at low Pb(II) concentrations with the synthesized sorbents was much higher than the reported results and, therefore, a higher efficiency of Pb(II) enrichment was achieved under acidic conditions.

Adsorption Kinetics

The kinetics of Pb(II) adsorption on Fe_3O_4@SiO_2-MnO_2(1.54) with different initial concentrations are depicted in **Figure 7A**. In roughly 30 min, equilibrium was reached at both initial concentrations of 10.0 and 25.0 mg L^{-1} of Pb(II) on the adsorbent. Adsorption kinetics can be better understood using three kinetic models (Yang et al., 2018): the pseudo-first-order model (**Eq. 5**), the pseudo-second-order model (**Eq. 6**), and the Weber-Morris model (**Eq. 7**).

$$\log(q_e - q_t) = \log q_e - \frac{k_1 t}{2.303} \tag{5}$$

$$\frac{t}{q_t} = \frac{1}{k_2 q_e^2} + \frac{t}{q_e} \tag{6}$$

$$q_t = k_d t^{1/2} + I \tag{7}$$

where the q_t (mg g^{-1}) is the adsorption amount at time t (min), k_1 (min^{-1}) is the pseudo-first-order rate constant, k_2 (g mg^{-1} min^{-1}) is pseudo-second-order rate constant, k_d and I denote the diffusion constant and the thickness of the boundary layer, respectively.

Figures 7B,C show change curves of log(q_e - q_t) with t and t/q_t with t; **Table 3** contains the fitting parameters. The kinetic results for Pb(II) adsorption onto Fe_3O_4@SiO_2-MnO_2(1.54) fit this pseudo-second-order kinetic model very well, showing that Pb(II) adsorption is pseudo-second-order and chemisorption-limited (Panahandeh et al., 2021). Pb(II) adsorbed over Fe_3O_4@SiO_2-MnO_2(1.54) was shown to adhere to pseudo-second-order kinetics when the slopes of the t/q_t against t plots were used. The projected q'_{cal} significant values were very close to the experimental values. There were slower adsorption rates with higher initial Pb(II) concentrations for the Pb(II) adsorption rate constants at 10.0 and 25.0 mg L^{-1} starting concentrations of Pb(II).

The fitted results of Pb(II) adsorption using Weber-Morris model are shown in **Figure 7D**, and the parameters that best fit the data are listed in **Table 3**. The plots display multilinearity with different initial Pb(II) concentrations, indicating that more than two procedures are involved in the adsorption. In **Figure 7D**, the Weber-Morris plots had two linear portions. The first is assigned to the fast adsorption of Pb(II), and the other to the function of the adsorption equilibrium. According to the model, if the adsorption process is mainly controlled by intraparticle diffusion, the q_t - $t^{1/2}$ plot will be a straight line passing through the origin (Yang et al., 2018). However, the first portion did not pass through initially indicate that external diffusion played a significant role in the adsorption procedure. Additionally, the intercepts decreased at high initial

concentrations, suggesting that the diffusion was not substantially affected by the mass transfer resistance. With initial Pb(II) concentrations of 10.0 and 25.0 mg L^{-1}, respectively, the k_d were 5.5 and 7.5 mg g^{-1} $min^{-1/2}$, indicating a higher diffusion constant at a higher initial concentration. This is likely due to the increasing diffusion driving force caused by the increasing concentration gradient.

Impact of Solution Chemistry on Pb(II) adsorption

The impact of the solution pH on Pb(II) adsorption by Fe_3O_4@SiO_2-MnO_2(1.54) is presented in **Figure 8**. The Pb(II) adsorption amount monotonically increased from 0.2 to 48.8 mg g^{-1} in the pH range from 2.0 to 8.0; subsequently, it remained constant. The pH effect on Pb(II) adsorption could be explained by the electrostatic interaction between the adsorbent and Pb(II), and the precipitation of Pb(II) at high pH conditions (>6.0) (Zhang et al., 2017b). Notably, SiO_2 based shell were not stable against alkaline condition. Although the Pb(II) adsorption capacity of the Fe_3O_4@SiO_2-MnO_2(1.54) was relatively high under high pH conditions, each adsorption performance test in this study was conducted at pH = 4.0 ± 0.2. Generally, the Fe_3O_4@SiO_2-MnO_2(1.54) surface was actively charged at solution pH values under the IEP of 1.4; electrostatic repulsive interaction occurred between Pb(II) and the protonated hydroxyl groups (Wang et al., 2020). In contrast, the adsorption sites were negatively charged at solution pH values above the IEP of 1.4, leading to an electrostatic attraction between deprotonated Mn-OH groups and Pb(II) (Zhang et al., 2020b), enhancing the Pb(II) adsorption.

Alkaline/Earth metal ions in natural water and wastewater may compete against Pb(II) for available adsorption sites of sorbents. The impacts of co-existing Na^+ and Ca^{2+} on Pb(II) adsorption are shown in **Figure 9A**. These electrolytes resulted in an increase in the Pb(II) adsorption, and Ca^{2+} had a more significant impact on adsorption than Na^+ did, suggesting that Pb(II) adsorption was controlled mainly by a surface complexation model (Zhang et al., 2020b). Notably, the effects of co-existing Na^+ and Ca^{2+} on Pb(II) adsorption revealed the presence of a preferable adsorbent, which exhibited great potential for Pb(II) treatment in the presence of co-existing cations at high concentrations.

In aquatic systems, dissolved humic acid may have an effect on the adsorption of Pb(II) (Esfandiar et al., 2022). **Figure 9B** depicts the adsorption isotherms of Pb(II) on Fe_3O_4@SiO_2-MnO_2(1.54) in the absence and presence of dissolved humic acid at a concentration of 10.2 mg L^{-1}. The results indicate the active effect of dissolved humic acid on Pb(II) adsorption at higher equilibrium Pb(II) concentrations under the tested conditions. This positive effect is attributed to the formation of weakly adsorbing complexes between Pb(II) and humic acid (Zhang et al., 2017a).

Regeneration and Reuse of the Adsorbent

Based on the finding that Fe_3O_4@SiO_2-MnO_2 had a poor adsorption capacity at low pH values, the Pb(II)-saturated adsorbent was thought to be regenerated through the acid treatment. The adsorbent was reused for eight adsorption-regeneration periods and the results are displayed in **Figure 10**. The adsorption capacity reduced from 31.4 to 25.6 mg g^{-1} during the initial four adsorption-desorption cycles, likely because of partial active species loss during cycle processes or the incomplete desorption of Pb(II) from the surface of Fe_3O_4@SiO_2-MnO_2(1.54). After four cycles, the Fe_3O_4@SiO_2-MnO_2(1.54) adsorption capacity remained constant, and the sorbent could be efficiently separated from the solution within 10 s by an external magnetic field, indicating that the sorbent was stable and recyclable.

Implication for Real-World Application

Efficient removal of Pb(II) in wastewater and rapid separation of adsorbents have always been the difficulties in the practical application of adsorbents. The as-prepared Fe_3O_4@SiO_2-MnO_2 showed high adsorption capacity and good stability for Pb(II) adsorptive removal from acidic Pb(II)-contaminated water, suggesting potential application in wastewater treatment field. Additionally, after adsorbing Pb(II) in wastewater the effective separation and recovery of Fe_3O_4@SiO_2-MnO_2 adsorbent could be accomplished within seconds with an external magnetic field. Furthermore, the Fe_3O_4@SiO_2-MnO_2 adsorbent could be rapidly redispersed while the magnetic field was removed. This means that only one external magnetic field can be used to quickly and efficiently realize the adsorption and desorption of Pb(II) by the adsorbent, which is beneficial to reduce the cost of adsorptive removal of Pb(II) in wastewater.

CONCLUSION

In this research, magnetic core-shell sorbents of Fe_3O_4@SiO_2-MnO_2 with various MnO_2 deposition contents were synthesized through deposition-precipitation and used for Pb(II) adsorption. The characterization results revealed that the Fe_3O_4 core was coated by a rough silica shell and a relatively loose MnO_2 deposition. Accordingly, Fe_3O_4@SiO_2-MnO_2 demonstrated increased Pb(II) adsorption in comparison to Fe_3O_4@SiO_2, and the Pb(II) adsorption amount was positively related to the MnO_2 deposition level. Fe_3O_4@SiO_2-MnO_2 could be easily divided and recovered using an outer magnetic component. The sorbent exhibited stable adsorption and regeneration performance after four consecutive adsorption-desorption periods. This adsorption was contained by surface complexation and slightly enhanced by dissolved humic acid and co-existing cations. These findings highlight that Fe_3O_4@SiO_2-MnO_2 is a promising adsorbent for use in the removal of Pb(II) from water and wastewater.

DATA AVAILABILITY STATEMENT

The original contributions presented in the study are included in the article/Supplementary Material, further inquiries can be directed to the corresponding author.

AUTHOR CONTRIBUTIONS

HZ contributed to data curation, methodology, writing-original draft, and writing-review and editing; SC contributed to data curation and investigation; YS and JW designed all experiments and revised and examined the manuscript; XQ contributed to review and editing; YY contributed to review and editing. All authors have read and agreed to the published version of the manuscript.

FUNDINGS

This work was supported by the National Natural Science Foundation of China (31872179, 31901447, 41701093), the Key R&D Plan Program of Jiangsu Province (BE2020319), the Innovation and Entrepreneurship Program of Jiangsu Province (JSSCBS20211062), the Excellent Doctor in Lvyangjinfeng of Yangzhou City (YZLYJFJH2021YXBS155), and the Blue Project of Yangzhou University.

REFERENCES

Bandar, S., Anbia, M., and Salehi, S. (2021). Comparison of MnO_2 Modified and Unmodified Magnetic Fe_3O_4 Nanoparticle Adsorbents and Their Potential to Remove Iron and Manganese from Aqueous Media. *J. Alloys Compd.* 851, 156822. doi:10.1016/j.jallcom.2020.156822

Chen, Y., Wang, M., Hu, Y., and Han, J. (2018). Poly(2-Aminothiophenol)/MnO_2 Hierarchical Nanocables as Efficient Adsorbents towards Heavy Metal Ions. *Mater. Chem. Phys.* 214, 172–179. doi:10.1016/j.matchemphys.2018.04.076

Esfandiar, N., Suri, R., and Mckenzie, E. R. (2022). Competitive Sorption of Cd, Cr, Cu, Ni, Pb and Zn from Stormwater Runoff by Five Low-Cost Sorbents; Effects of Co-Contaminants, Humic Acid, Salinity and pH. *J. Hazard. Mater.* 423, 126938. doi:10.1016/j.jhazmat.2021.126938

FaheemYu, H. X., Liu, J., Shen, J. Y., Sun, X. Y., Li, J. S., et al. (2016). Preparation of MnO_x-Loaded Biochar for Pb^{2+} Removal: Adsorption Performance and Possible Mechanism. *J. Taiwan Inst. Chem. Eng.* 66, 313–320. doi:10.1016/j.jtice.2016.07.010

Ghaedi, S., Seifpanahi-Shabani, K., and Sillanpää, M. (2022). Waste-to-resource: New Application of Modified Mine Silicate Waste to Removal Pb^{2+} Ion and Methylene Blue Dye, Adsorption Properties, Mechanism of Action and Recycling. *Chemosphere* 292, 133412. doi:10.1016/j.chemosphere.2021.133412

Gugushe, A. S., Mpupa, A., Munonde, T. S., Nyaba, L., and Nomngongo, P. N. (2021). Adsorptive Removal of Cd, Cu, Ni and Mn from Environmental Samples Using Fe_3O_4-ZrO_2@APS Nanocomposite: Kinetic and Equilibrium Isotherm Studies. *Molecules* 26, 3209. doi:10.3390/molecules26113209

Hamid, S. A., Azha, S. F., Sellaoui, L., Bonilla-Petriciolet, A., and Ismail, S. (2020). Adsorption of Copper(II) Cation on Polysulfone/zeolite Blend Sheet Membrane: Synthesis, Characterization, Experiments and Adsorption Modelling. *Colloids Surfaces A Physicochem. Eng. Aspects* 601, 124980. doi:10.1016/j.colsurfa.2020.124980

Huang, S., Gu, L., Zhu, N., Feng, K., Yuan, H., Lou, Z., et al. (2014). Heavy Metal Recovery from Electroplating Wastewater by Synthesis of Mixed-Fe_3O_4@SiO_2/metal Oxide Magnetite Photocatalysts. *Green Chem.* 16, 2696–2705. doi:10.1039/C3GC42496K

Hussain, T., Hussain, A. I., Chatha, S. A. S., Ali, A., Rizwan, M., Ali, S., et al. (2021). Synthesis and Characterization of Na-Zeolites from Textile Waste Ash and its Application for Removal of Lead (Pb) from Wastewater. *Int. J. Environ. Res. Public Health* 18, 3373. doi:10.3390/ijerph18073373

Li, Q., Fu, L., Wang, Z., Li, A., Shuang, C., and Gao, C. (2017). Synthesis and Characterization of a Novel Magnetic Cation Exchange Resin and its Application for Efficient Removal of Cu^{2+} and Ni^{2+} from Aqueous Solutions. *J. Clean. Prod.* 165, 801–810. doi:10.1016/j.jclepro.2017.06.150

Li, W., Li, Y., Liu, J., Chao, S., Yang, T., Li, L., et al. (2021). A Novel Hollow carbon@MnO_2 Electrospun Nanofiber Adsorbent for Efficient Removal of Pb^{2+} in Wastewater. *Chem. Res. Chin. Univ.* 37, 496–504. doi:10.1007/s40242-021-1085-7

Li, M., Kuang, S., Kang, Y., Ma, H., Dong, J., and Guo, Z. (2022). Recent Advances in Application of Iron-Manganese Oxide Nanomaterials for Removal of Heavy Metals in the Aquatic Environment. *Sci. Total Environ.* 819, 153157. doi:10.1016/j.scitotenv.2022.153157

Liu, X., Bai, X., Dong, L., Liang, J., Jin, Y., Wei, Y., et al. (2018). Composting Enhances the Removal of Lead Ions in Aqueous Solution by Spent Mushroom Substrate: Biosorption and Precipitation. *J. Clean. Prod.* 200, 1–11. doi:10.1016/j.jclepro.2018.07.182

McBride, M. B. (1997). A Critique of Diffuse Double Layer Models Applied to Colloid and Surface Chemistry. *Clays Clay Minerals* 45, 598–608. doi:10.1346/CCMN.1997.0450412

Minale, M., Gu, Z., Guadie, A., Li, Y., Wang, Y., Meng, Y., et al. (2021). Hydrous Manganese Dioxide Modified Ploy(sodium Acrylate) Hydrogel Composite as a Novel Adsorbent for Enhanced Removal of Tetracycline and Lead from Water. *Chemosphere* 272, 129902. doi:10.1016/j.chemosphere.2021.129902

Panahandeh, A., Parvareh, A., and Moraveji, M. K. (2021). Synthesis and Characterization of γ-MnO_2/chitosan/Fe_3O_4 Cross-Linked with EDTA and the Study of its Efficiency for the Elimination of Zinc(II) and Lead(II) from Wastewater. *Environ. Sci. Pollut. Res.* 28, 9235–9254. doi:10.1007/s11356-020-11359-x

Shi, Y., Han, Z., Yang, J., and Meng, Q. (2021). Influence of the Hollowness and Size Distribution on the Magnetic Properties of Fe_3O_4 Nanospheres. *Langmuir* 37, 9605–9612. doi:10.1021/acs.langmuir.1c01498

Vishnu, D., and Dhandapani, B. (2020). Integration of *Cynodon Dactylon* and *Muraya Koenigii* Plant Extracts in Amino-Functionalised Silica-Coated Magnetic Nanoparticles as an Effective Sorbent for the Removal of Chromium(VI) Metal Pollutants. *IET Nanobiotechnol.* 14, 449–456. doi:10.1049/iet-nbt.2019.0313

Wan, S., Wu, J., Zhou, S., Wang, R., Gao, B., and He, F. (2018). Enhanced Lead and Cadmium Removal Using Biochar-Supported Hydrated Manganese Oxide (HMO) Nanoparticles: Behavior and Mechanism. *Sci. Total Environ.* 616-617, 1298–1306. doi:10.1016/j.scitotenv.2017.10.188

Wan, S., Qiu, L., Li, Y., Sun, J., Gao, B., He, F., et al. (2020). Accelerated Antimony and Copper Removal by Manganese Oxide Embedded in Biochar with Enlarged Pore Structure. *Chem. Eng. J.* 402, 126021. doi:10.1016/j.cej.2020.126021

Wang, W., Zhou, J., Wei, D., Wan, H., Zheng, S., Xu, Z., et al. (2013). ZrO_2-functionalized Magnetic Mesoporous SiO_2 as Effective Phosphate Adsorbent. *J. Colloid Interface Sci.* 407, 442–449. doi:10.1016/j.jcis.2013.06.053

Wang, S., Gao, B., Li, Y., Mosa, A., Zimmerman, A. R., Ma, L. Q., et al. (2015a). Manganese Oxide-Modified Biochars: Preparation, Characterization, and Sorption of Arsenate and Lead. *Bioresour. Technol.* 181, 13–17. doi:10.1016/j.biortech.2015.01.044

Wang, W., Zhang, H., Zhang, L., Wan, H., Zheng, S., and Xu, Z. (2015b). Adsorptive Removal of Phosphate by Magnetic Fe_3O_4@C@ZrO_2. *Colloids Surfaces A Physicochem. Eng. Aspects* 469, 100–106. doi:10.1016/j.colsurfa.2015.01.002

Wang, B., Yu, J., Liao, H., Zhu, W., Ding, P., and Zhou, J. (2020). Adsorption of Lead(II) from Aqueous Solution with High Efficiency by Hydrothermal Biochar Derived from Honey. *Int. J. Environ. Res. Public Health* 17, 3441. doi:10.3390/ijerph17103441

Xia, W., and Liu, Y. (2021). Preparation of MnO_2 Modified Magnetic Graphitic Carbon Nitride Composite and its Adsorption toward Pb(II) in Waste Water. *Water Pract. Technol.* 16, 1498–1509. doi:10.2166/wpt.2021.059

Xu, W., Song, Y., Dai, K., Sun, S., Liu, G., and Yao, J. (2018). Novel Ternary Nanohybrids of Tetraethylenepentamine and Graphene Oxide Decorated with $MnFe_2O_4$ Magnetic Nanoparticles for the Adsorption of Pb(II). *J. Hazard. Mater.* 358, 337–345. doi:10.1016/j.jhazmat.2018.06.071

Yadav, P., Farnood, R., and Kumar, V. (2021). HMO-incorporated Electrospun Nanofiber Recyclable Membranes: Characterization and Adsorptive Performance for Pb(II) and As(V). *J. Environ. Chem. Eng.* 9, 106507. doi:10.1016/j.jece.2021.106507

Yang, Y., Wang, J., Qian, X., Shan, Y., and Zhang, H. (2018). Aminopropyl-functionalized Mesoporous Carbon (APTMS-CMK-3) as Effective Phosphate Adsorbent. *Appl. Surf. Sci.* 427, 206–214. doi:10.1016/j.apsusc.2017.08.213

Yin, H., Liu, F., Feng, X., Liu, M., Tan, W., and Qiu, G. (2011). Co^{2+}-exchange Mechanism of Birnessite and its Application for the Removal of Pb^{2+} and As(III). *J. Hazard. Mater.* 196, 318–326. doi:10.1016/j.jhazmat.2011.09.027

Zhang, L., Yang, X., and Wu, Y. (2015). Synthesis of Fe_3O_4@SiO_2@MnO_2 Composite Magnetic Submicrospheres as Adsorbent for Methyl Orange Decolouration. *Micro & Nano Lett.* 10, 12–15. doi:10.1049/mnl.2014.0555

Zhang, H., Gu, L., Zhang, L., Zheng, S., Wan, H., Sun, J., et al. (2017a). Removal of Aqueous Pb(II) by Adsorption on Al_2O_3-Pillared Layered MnO_2. *Appl. Surf. Sci.* 406, 330–338. doi:10.1016/j.apsusc.2017.02.011

Zhang, H., Wu, A., Fu, H., Zhang, L., Liu, H., Zheng, S., et al. (2017b). Efficient Removal of Pb(II) Ions Using Manganese Oxides: the Role of Crystal Structure. *RSC Adv.* 7, 41228–41240. doi:10.1039/C7RA05955H

Zhang, H., Xu, F., Xue, J., Chen, S., Wang, J., and Yang, Y. (2020a). Enhanced Removal of Heavy Metal Ions from Aqueous Solution Using Manganese Dioxide-Loaded Biochar: Behaviour and Mechanism. *Sci. Rep.* 10, 6067. doi:10.1038/s41598-020-63000-z

Zhang, H., Yang, Y., Yuan, L., Liu, G., Shan, Y., Qian, X., et al. (2020b). Improving the Lead Adsorption Performance of Mesoporous MnO_2 by Plasma Surface Modification. *Dwt* 189, 283–295. doi:10.5004/dwt.2020.25607

Zhu, J., Baig, S. A., Sheng, T., Lou, Z., Wang, Z., and Xu, X. (2015). Fe_3O_4 and MnO_2 Assembled on Honeycomb Briquette Cinders (HBC) for Arsenic Removal from Aqueous Solutions. *J. Hazard. Mater.* 286, 220–228. doi:10.1016/j.jhazmat.2015.01.004

Zhu, S., Lin, X., Dong, G., Yu, Y., Yu, H., Bian, D., et al. (2019). Valorization of Manganese-Containing Groundwater Treatment Sludge by Preparing Magnetic Adsorbent for Cu(II) Adsorption. *J. Environ. Manag.* 236, 446–454. doi:10.1016/j.jenvman.2019.01.117

Conflict of Interest: The authors declare that the research was conducted in the absence of any commercial or financial relationships that could be construed as a potential conflict of interest.

Publisher's Note: All claims expressed in this article are solely those of the authors and do not necessarily represent those of their affiliated organizations, or those of the publisher, the editors and the reviewers. Any product that may be evaluated in this article, or claim that may be made by its manufacturer, is not guaranteed or endorsed by the publisher.